



Modeling of temperature distribution and clad geometry of the molten pool during laser cladding of CoCrCuFeNi alloys

Dachuan Tian¹ · Chonggui Li¹ · Zhiguo Hu¹ · Xintong Li¹ · Yajun Guo¹ · Xiaosong Feng² · Zhenhai Xu³ · Xiaoguang Sun⁴ · Wenge Li⁵

Received: 5 December 2022 / Accepted: 8 April 2024 / Published online: 15 April 2024
© The Author(s), under exclusive licence to Springer-Verlag London Ltd., part of Springer Nature 2024

Abstract

This work simulated a modified three-dimensional single-track finite element model and a temperature discrimination mechanism in order to investigate the variation of temperature field in stainless steel and the effect of technological parameters on the coating. Through theoretical calculation, the distinction between the thermal characteristics of CoCrCuFeNi powders and CoCrCuFeNi alloys was made to improve the precision of simulation findings. In addition, to more precisely represent the heat transfer, an asymmetric Gaussian was used to distributed heat source and exponentially change the laser energy to account for the attenuation of laser power along the z-axis. The absorption rate of the laser beam at different temperatures of the material was also considered. The data was curve-fitted to examine the impact of laser power and scanning speed on the cladding layer morphologies. The laser power was found to be proportional to the width and depth of the clad layer, whereas the laser scanning speed was found to be inversely related to the width and depth of the clad layer. The simulation results were basically matched to the experiment.

Keywords Laser cladding · Temperature distribution · High entropy alloys · Clad geometry · Simulation

1 Introduction

As a traditional engineering material, 304 stainless steel are widely utilized in various fields due to their high corrosion resistance, low cost, and superior mechanical processing qualities [1–3]. However, the low hardness of this stainless steel results in poor surface wear resistance, which makes it unsuitable for frictional wear conditions. This disadvantage severely restricts its applicability [4]. Laser

cladding technology use a high-energy laser beam to melt the substrate and alloy or non-metallic powder, which is then rapidly cooled to produce a novel surface modification technique for coating. Compared to conventional coating technology for metal surface preparation, laser cladding technology can effectively improve material strength, hardness, wear resistance, corrosion resistance, and other qualities, and its heat-affected zone is smaller and its performance is more tunable [5]. Consequently, the combination of laser cladding technology and high entropy alloy to produce an alloy coating can effectively increase the wear resistance of 304 stainless steel.

CoCrCuFeNi high entropy alloys (HEAs) are one of the most important forms of HEAs, and their unique microstructure has garnered much attention [6–8]. The high entropy effect, lattice distortion effect, diffusion hysteresis effect, and cocktail effect [9–11] confer on HEAs superior hardness, strength, corrosion resistance, wear resistance, and thermal stability compared to normal alloys.

The single track is the smallest part unit in the laser cladding process, and the study of the single track's characteristics has a significant effect on the part accuracy [12]. For single-track laser cladding, the process

✉ Chonggui Li
chongguili@sues.edu.cn

¹ School of Materials Science and Engineering, Shanghai University of Engineering Science, Shanghai 201620, China

² Shanghai Aerospace Equipment Manufacturer Co., Ltd., Shanghai 200245, China

³ National Key Laboratory for Precision Hot Processing of Metals, Harbin Institute of Technology, Harbin 150001, China

⁴ Technical Engineering Department, CRRC Qingdao Sifang Co. Ltd., Qingdao 266111, China

⁵ Institute for Marine Materials Science and Engineering, Shanghai Maritime University, Shanghai 201306, China

parameters (powder feed rate, scanning speed, laser power, and material characteristics) typically have a significant impact on the shape and coating quality of the final clad layer [13, 14]. Li et al. [15] studied the effect of remelting scanning rates on the capacity of laser-clad Ni-based coatings to generate amorphous structures. Ma et al. [16] combined principal component analysis (PCA) with the TOPSIS method, and through the study of AISi 1040, determined that the laser power had the greatest impact on the quality of the cladding layer in the laser cladding process parameters, and that this method could obtain the optimal solution of the process parameters.

Since the environment of the high-temperature melting and quick cooling processes in laser melting is harsh and difficult to monitor, the reproduction of the physical processes using numerical models can save experimental cycles and costs [17]. Lei et al. [18] investigated the temperature field distribution, temperature profiles at various nodes, and the nucleation, growth rate, and size of TiC particles were evaluated using the temperature profiles, and the theoretical and experimental results largely agreed. Gao et al. [19] established a single-track laser melting prediction model based on the birth–death element method and Gaussian heat source distribution, and the prediction results were less than 6.6% error in the width and height of the melting layer and less than 3.0% error in the maximum temperature compared with the experimental results, while The effect of the radical scanning speed on the geometry of the molten layer was investigated, and it was discovered that the height of the molten layer decreased with increasing radical scanning. Hofman et al. [20] suggested a new cladding model to investigate the link between laser cladding process parameters and dilution rate, and the simulated results matched the experimental findings. They discovered that the level of dilution decreased when the width of the melt element was less than the critical width, which was approximately 90 percent of the laser beam's diameter.

Numerous researches combine numerical simulations with tests to examine the effect of laser melting process parameters on the quality of the melted coating, as well as curve fitting of the simulated data to predict the morphology of the melted coating. The innovation of this article is to propose an improved three-dimensional model using an asymmetric Gaussian-distributed heat source to investigate the influence of laser rate and scanning speed on single-track laser melting coatings. In this paper, considering the laser power decay of the powder layer in the model built in and the material for the laser power absorption. The data were curve-fitted to predict the cladding layer morphology, which basically agrees with the actual test comparison.

2 Materials and experiments

2.1 Preparation of material

CoCrCuFeNi HEAs were chosen as cladding materials for simulation, the specific composition is shown in Table 1. The base material was selected as 304 stainless steel; the specific composition is shown in Table 2 [21, 22]. Parameter simulation simulated is shown in Table 3.

To determine the powder's thermal properties at high temperatures, high entropy alloy was created, and the density of the powder was estimated at room temperature. CoCrCuFeNi alloy was obtained by mixing 20% Co, 20% Cr powder, 20% Cu powder, and 20% Mn powder. The alloy powder and abrasion (Agate balls) to be processed was placed in the grinding ball tank, and fixed in the planetary grinder for thorough mixing. The equipment and principles of the planetary grinder are shown in Fig. 1. Finally, in order to remove the moisture from the powder, the uniformly mixed powder was placed in the pot and put in the oven to dry for 2–3 h.

Due to the harshness of the high temperature environment, the JMatPro software was used to simulate and calculate the thermal properties of the alloy. The properties of the powder state are different from the alloy state. Therefore, the thermal properties of alloy powder state were computed independently. The density of the powder can be concluded as follows [23]:

$$\rho = \eta\rho_g + (1 - \eta)\rho_s \quad (1)$$

where η is the porosity of the powder, ρ_g is the density of the gas, and ρ_s is the density of the high entropy alloy.

The density of the actual high-entropy alloy powders measured at room temperature is 6565.8 kg/m³ and the software calculated the density of the CoCrCuFeNi HEAs as 8323.9 kg/m³. The procedure for measuring the density of actual high-entropy alloy powders is shown in Fig. 2.

The calculated porosity η is about 25%. The Gusarov model [24] shows that the porosity of the powder has an effect on the thermal conductivity of the material, and considering the porosity of the powder, the thermal conductivity of the material can be expressed as:

$$k_e = k \frac{(1 - \eta)n a}{\pi R} \quad (2)$$

where k is the thermal conductivity of the CoCrCuFeNi HEAs, η is the porosity of the CoCrCuFeNi HEAs powder, n is the coordination number, a is the sintering neck radius

Table 1 Main chemical composition of high entropy alloys(wt.%)

Element	Co	Cu	Cr	Fe	Ni
Content	20	20	20	20	20

Table 2 Main chemical composition of 304 stainless steel(wt.%)

Element	C	Si	Mn	Cr	Ni	S	P	Fe
Content	≤0.08	≤1.0	≤2.0	18.0~20.0	8.0~10.0	≤0.03	≤0.045	Bal

Table 3 Process parameters for laser cladding experiments

Number	Laser power (W)	Scanning speed (mm/s)
1	1000	10
2	1250	10
3	1500	5
4	1500	7.5
5	1500	10
6	1500	12.5
7	1750	10
8	2000	10

of the powder, and R is the average radius of the powder, as Fig. 3 shows the thermophysical properties of the high-entropy alloy powder with the alloy state.

2.2 Preparation of coatings

To verify the accuracy of the model, experiments were run. The YLS-5000 fiber laser manufactured by IPG was used to prepare cladding coatings. Figure 4 shows the laser cladding process. Before laser processing, the specimen was fixed to the processing table with a fixture, and the processing start and end points was calibrated. At the same time, the laser power, defocus amount, and scanning speed was set. After all personnel had left the room, the cladding test was completed by the computer-controlled processing program. Ar gas with a conveying volume of 15 L/min was utilized during laser processing to separate the air around

the specimen which ensured the molten pool that results was not oxidized. Table 3 shows the parameter settings for the simulation.

3 Mathematical modeling of single-track laser cladding

3.1 Model building and meshing

The schematic diagram for this paper's finite element analysis is provided in Fig. 5. A symmetric model was built to reduce the amount of computation. Figure 6 shows the model which constructed by the ANSYS 18.0 software. The dimensions are 20 mm, 4 mm, and 2.5 mm. It is the transverse cross-sectional view and longitudinal cross-sectional view of the model, distinguished by different colors according to the material: the green area represents high entropy alloy powder, the red area represents powder that has transformed the alloy state, and the purple area represents the 304 stainless steel substrate. The element type of the model used SOLID70 which is a three-dimensional heat transfer element with eight nodes and one degree of freedom per node. The current temperature of a single element was determined by averaging the temperatures of its nodes. Temperature discrimination mechanism was used to achieve the transformation of powder element to alloy element while the temperature above the alloy's melting point. The discrimination mechanism was characterized as follows:

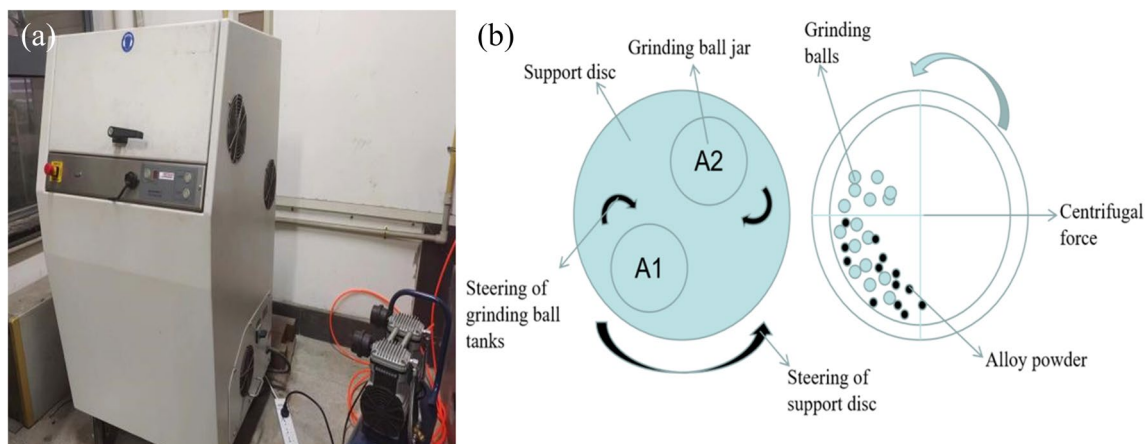


Fig. 1 Ball mill system: **a** experiment equipment, **b** schematic diagram

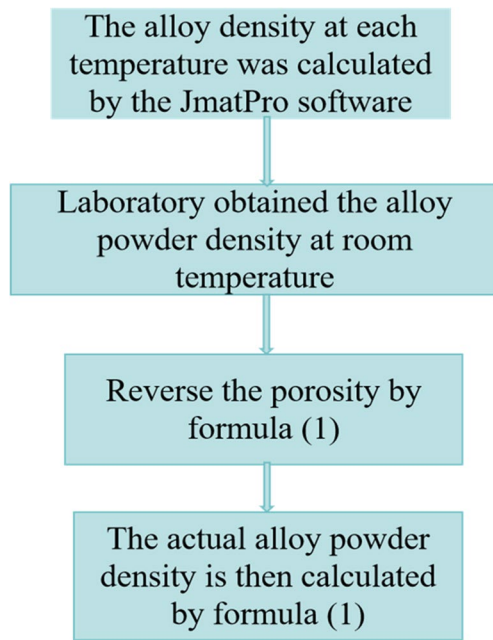


Fig. 2 The procedure for measuring the density of actual high-entropy alloy powders

$$T(i) = \frac{\sum_1^m T_m}{m} (m = 8) \quad (3)$$

$$\begin{cases} \text{for } i \text{ tok} \\ \text{if } T(i) < T_{melt} \\ \text{set } Mat = 1 \\ \text{or set } Mat = 2 \end{cases} \quad (4)$$

where $T(i)$ is the average temperature of each element, k is the total number of element in the cladding layer, 1 is the material properties of the high-entropy alloy powder, and 2 is the material properties of the high-entropy alloy.

In order to converge the solution results, the Newton-Laplacian solution option was used and a steady-state analysis was performed to obtain the boundary conditions before the final transient analysis.

Considering the latent heat of phase change, the differential equation of heat conduction for the transient temperature field in Cartesian coordinate system is shown in follows:

$$\frac{\partial}{\partial x}(K_x \frac{\partial T}{\partial x}) + \frac{\partial}{\partial y}(K_y \frac{\partial T}{\partial y}) + \frac{\partial}{\partial z}(K_z \frac{\partial T}{\partial z}) + \rho Q = \rho c \frac{\partial T}{\partial t} \quad (5)$$

where Q is the latent heat of phase transformations, c is the specific capacity, ρ is the density, and K_x , K_y , and K_z are the thermal conductivity in the direction of the width, length, and depth of the preset layer. T is the function of temperature distribution, and t is the time.

The temperature gradually grew from the surface to the bottom during the laser cladding process. This article assumed that heat conduction occurs at the bottom of the model and the other surfaces are heat transferring with the environment. Considering three types of heat conduction, heat convection, and heat radiation, which are mathematically expressed as follows:

$$T(x, y, z, t) = \bar{T}(t)(\Gamma_1) \quad (6)$$

$$K_x \frac{\partial T}{\partial x} n_x + K_y \frac{\partial T}{\partial y} n_y + K_z \frac{\partial T}{\partial z} n_z = \bar{q}_f(t)(\Gamma_2) \quad (7)$$

$$K_x \frac{\partial T}{\partial x} n_x + K_y \frac{\partial T}{\partial y} n_y + K_z \frac{\partial T}{\partial z} n_z = \bar{h}_c(T_e - T)(\Gamma_3) \quad (8)$$

$$K_x \frac{\partial T}{\partial x} n_x + K_y \frac{\partial T}{\partial y} n_y + K_z \frac{\partial T}{\partial z} n_z = \varepsilon \sigma (T_e^4 - T^4)(\Gamma_4) \quad (9)$$

where $\bar{T}(t)$ is the given temperature on boundary Γ_1 , $\bar{q}_f(t)$ is the given heat source on boundary Γ_2 , \bar{h}_c is the heat transfer coefficient between the object and its surroundings, ε is the emissivity, and σ is the Stefan-Boltzmann constant.

3.2 Simplification of the model and assumptions

Due to the complexity of the laser cladding procedure, it is necessary to simplify models and make certain assumptions for improved numerical modeling. Due to the symmetry of the model, this paper applied symmetry constraints along the symmetry axis to construct half of the model. The second assumption this essay makes about the experimental environment is as follows:

- 1) Assuming that the powder material is isotropic and ignore the powder evaporation of the cladding layer.
- 2) Assuming that the laser intensity distribution is Gaussian, the equation is as follows:

$$q(x, y, z) = \frac{6AQ_m}{\pi R^2 \pi^{\frac{1}{2}} h} e^{\left(\frac{-3x^2}{R^2} + \frac{-3y^2}{R^2} + \frac{-3z^2}{R^2}\right)} \quad (10)$$

where A is the laser absorption efficiency, Q_m (W) is the maximum heat at the center of the heat source, R (m) is the laser beam radius, and h (m) is the distance from the heat source to the powder surface.

- 3) Since the material undergoes a phase change during the high temperature phase resulting in a change in the thermal properties of the material, this article calculates the latent heat of melting as a material property with the following equation. The equation is as follow:

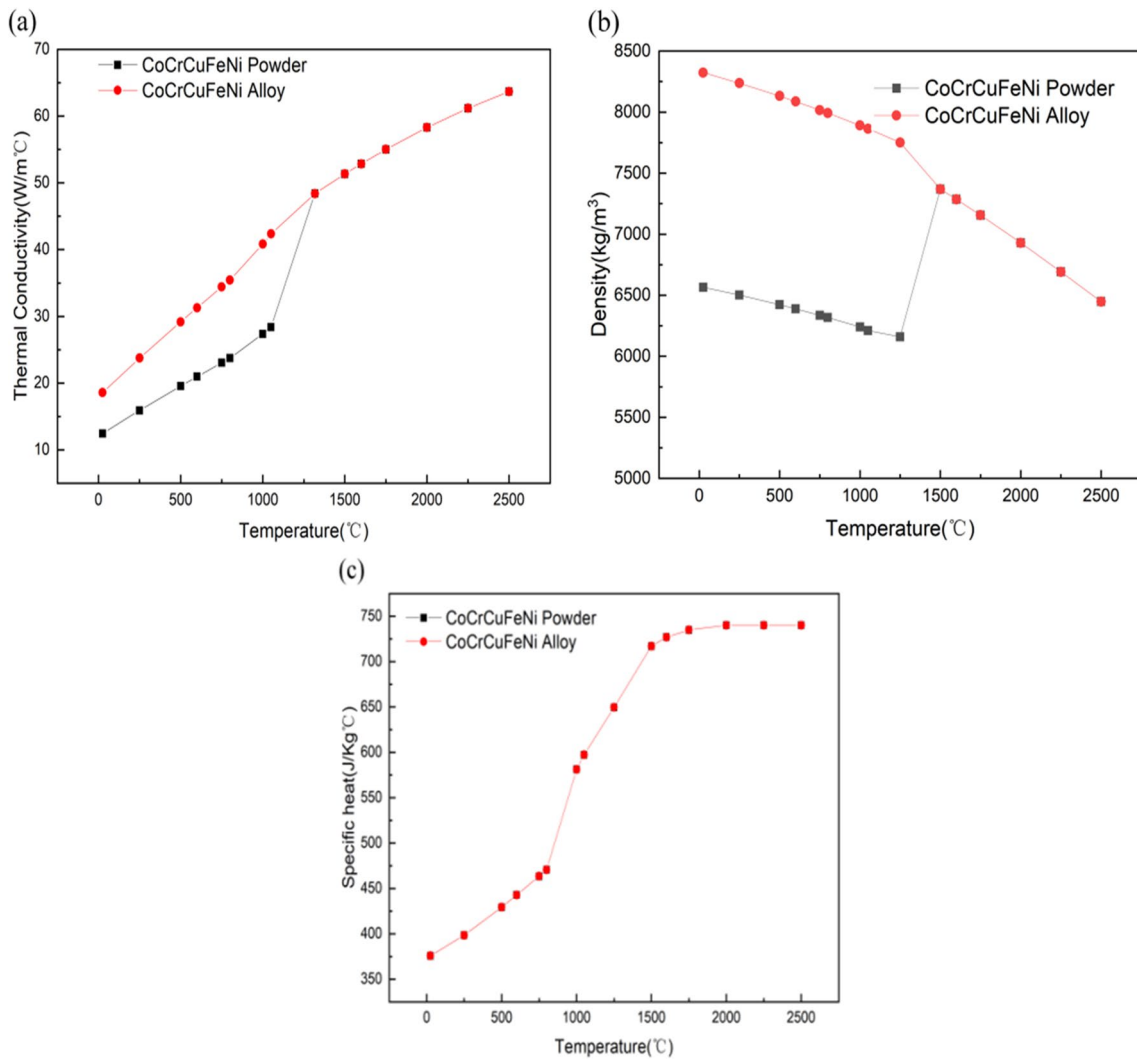


Fig. 3 Thermophysical properties at different temperature of CoCrCuFeNi powder and alloy: **a** thermal conductivity, **b** density, **c** specific heat

$$H = \int C dT \tag{11}$$

where T is the temperature and C is the specific heat capacity at the current temperature.

- Ignore the melt pool fluid, evaporative heat loss, and ignore non-melting heat transfer.

Considering that part of the energy is dissipated into the air by convection and radiation in the laser melting process, causing high intensity nonlinear calculation, the total heat transfer coefficient considering conventional and radiation is [25]:

$$\overline{h}_e = 24.1 \times 10^{-4} \epsilon T^{1.61} \tag{12}$$

where \overline{h}_e is the convective heat transfer coefficient and ϵ is the material emissivity.

3.3 Correction of the heat source model

Given that this paper examined a three-dimensional uniform heating body and used the high-energy additive laser cladding technology, the most accurate heat source model is the asymmetric Gaussian:

$$q(x, y, z) = \frac{6AQ_m}{\pi c^2 \pi^{\frac{1}{2}} h} e^{\left(\frac{-3x^2}{c^2} + \frac{-3y^2}{c^2} + \frac{-3z^2}{c^2}\right)} \tag{13}$$

where A is the laser absorption power, Q_m (W) is the maximum heat flow in the center of the heat source, c is the laser spot radius, and h is the distance between the heat source and the powder surface.

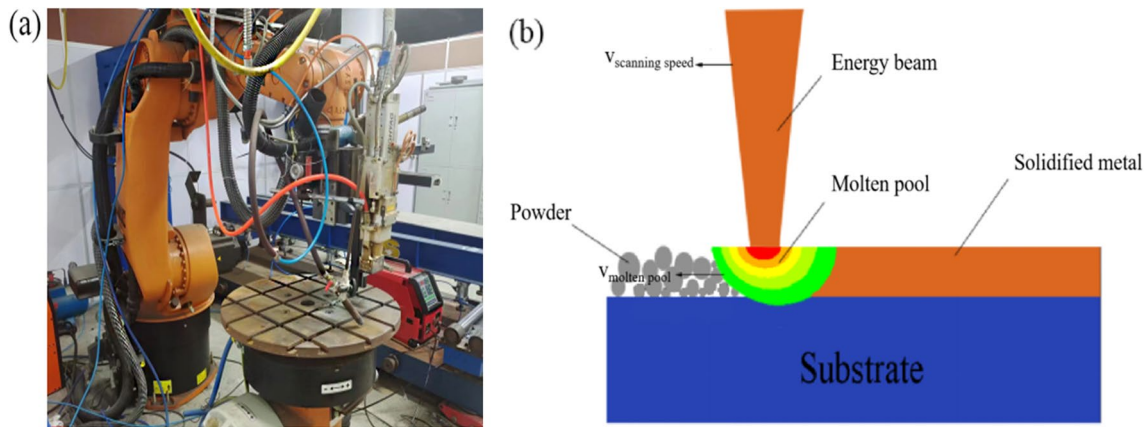


Fig. 4 Laser cladding system: **a** experiment equipment, **b** schematic diagram

Fig. 5 Flow chart of numerical simulation progress

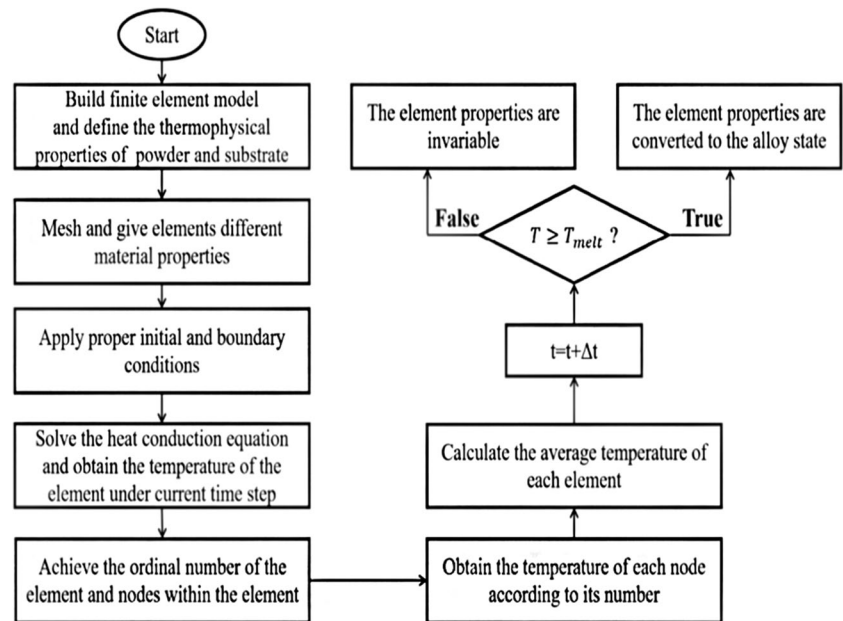


Fig. 6 Model geometry and grid of different attributes

Heat propagation in powder condition differs from that in alloy status due to the voids between the powder particles. It produces heat loss, which is mainly heat convection and heat radiation. Therefore, the laser energy was modified to match the actual situation. Due to the cladding powder layer, the attenuation of the laser in the z -axis direction was mainly considering. The attenuation formula is described as follows [26]:

$$I(x, y, z + \Delta z) = I(x, y, z) \left(\frac{3p\Delta C_e}{4p_p r_p} \right) \quad (14)$$

where I (J/m^3) is the density of laser energy, p is the concentration of the powder layer, p_p (kg/m^3) is the density of

Table 4 Resistivity of CoCrCuFeNi at different temperature

Temperature (°C)	25	250	500	750	1000	1250	1500	1750	2000
$\rho(10^{-6}\Omega \times m)$	0.38	0.52	0.62	0.71	0.74	0.74	0.82	0.86	0.92

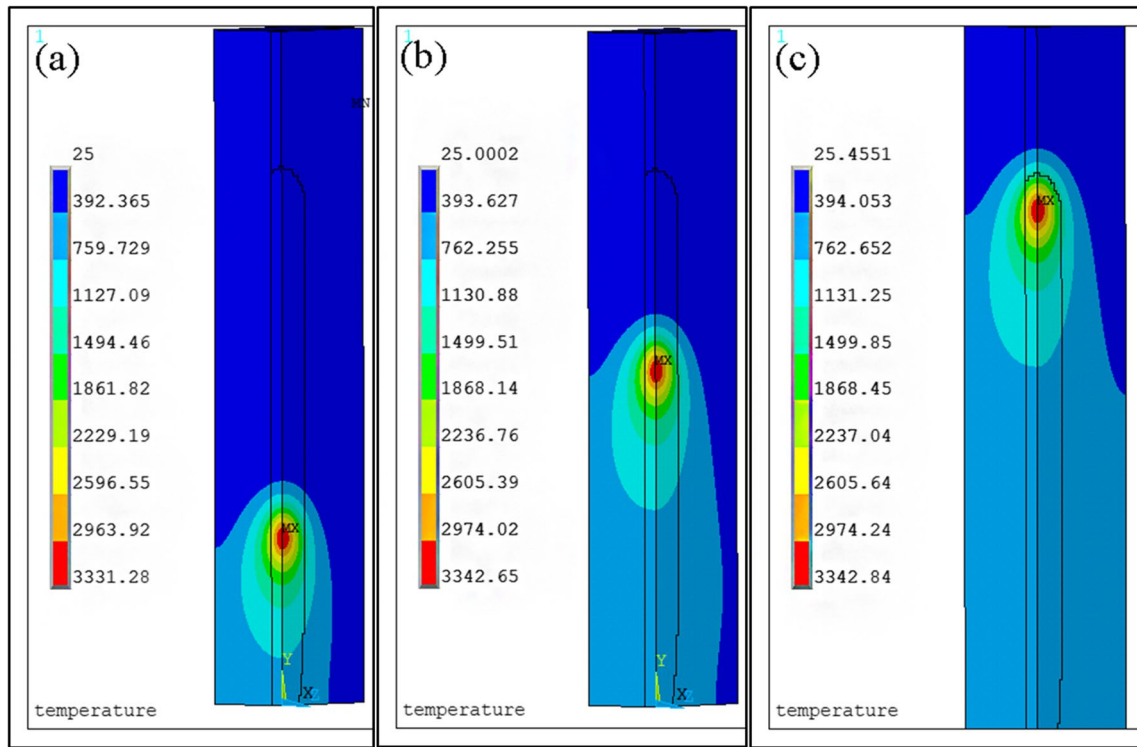


Fig. 7 Temperature distribution of the molten pool during simulation under laser power of 1500 W and scanning speed of 10 mm/s at different times: **a** 0.5 s, **b** 1.0 s, **c** 1.5 s

the powder layer, C_e is the extinction coefficient, and h (m) is the radius of the powder particles. The material expands at high temperatures, and the radius of the powder particles becomes larger, which increased the collision of the powder particles. This impact is not taken into account. The laser wavelength set by the experimental equipment is 1064 nm, and the value of C_e is selected as 11.2. Combined with Eq. (14) and Eq. (13), the heat source correction equation is expressed as follows:

$$q(x, y, z) = \frac{6AQ_m}{\pi R^2 \pi^{\frac{1}{2}} h} e^{\left(\frac{-3x^2}{R^2} + \frac{-3y^2}{R^2} + \frac{-3z^2}{h^2}\right)} e^{\frac{-3pzC_e}{4\rho_p\tau_p}} \quad (15)$$

In the laser cladding process, when the laser deposits more energy into the material, the thermophysical parameters of the material will change. The changes in these parameters will affect the absorption of laser energy by the material. The absorbed laser is mainly divided into two parts, on the one hand, when the laser irradiates the surface of the metal material, only a small part is absorbed by the

material because the free electrons of the metal reflect most of the laser; On the other hand, a small part of the laser light is absorbed by bound electrons and lattice vibrations within the metal. The absorption rate of the same material to the laser is affected by its physical property changes, for this reason it is necessary to consider the absorption rate A of the laser at different temperatures, as shown in the following equation [27]:

$$A = 0.1457 \frac{\rho}{\gamma} + 0.09e^{-0.5 \frac{\gamma - c}{\rho}} + \frac{\rho}{N\gamma - 1.0 \times 10^{-6}} \quad (16)$$

where N is the average number of extranuclear electron layers, γ is the wavelength of the incident wave (the wavelength of this device is 1064 nm), ρ is the resistivity, and c is a constant calculated by simulation. The material resistivity is a function of temperature, so the absorption rate Z of the laser beam by the material was regarded as a temperature function. The resistivity of the material calculated by software is shown in Table 4.

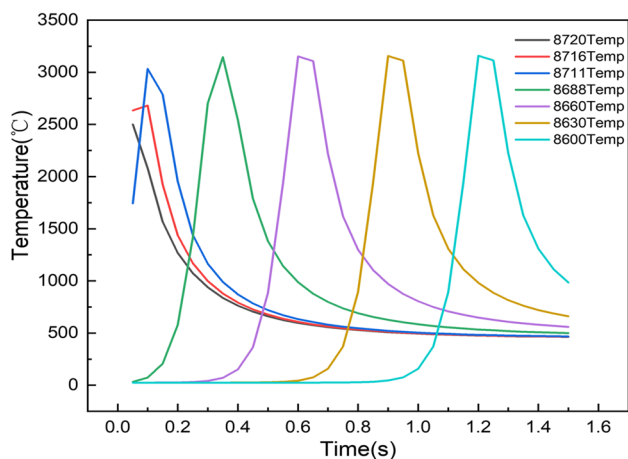


Fig. 8 Temperature curves at different nodes

4 Results and discussion

Figure 7 shows a cloud of temperature fields at various times, which used a laser power of 1500 W and a scanning speed of 10 mm/s. The black line in the illustration separates the melted and unmelted regions. It can be observed that the temperature was the highest in the center of the melt pool, and that the molten pool morphology had a Gaussian distribution. The maximum temperature for temperature clouds at various moments in time increased over time. It is because that heat conduction is the primary mode of heat transport within a material. When the laser beam irradiated to the surface of the material, the temperature of the irradiation center was constantly rising. However, because heat can only be transferred to one side at the end, accumulated heat was produced in a short amount of time. Accumulated heat was transferred in the direction of the laser scan, which caused the peak temperature to keep rising.

Figure 8 shows the variations in temperature over time at several nodes, which were all on the same straight line in the direction of laser scanning. The distance between nodes was proportional to the number of nodes between them. The laser began scanning at node 8720, and as the number of nodes reduced, the maximum value of change curve rised. The node temperature reached its maximum at node 8688, after which the node temperature curve tended to stabilize. After the laser beam began to illuminate the embedding layer, the results indicated that the thermal conductivity and temperature distribution attain a quasi-static state over a short distance. The rate of temperature change in the high temperature stage was substantially faster than in the low temperature stage. Furthermore, the rapid scanning speed considerably reduced heating and cooling durations. The heat intake was mostly relied on

thermal conduction, implying that thermal conductivity was more efficient at higher temperatures [18].

4.1 Effect of different laser power on cladding layer

In order to research how the topography of the cladding layer is affected by laser power, monitoring points was selected with laser power of 1000 W, 1250 W, 1500 W, 1750 W, and 2000 W in the horizontal direction, as shown in Fig. 9. The monitoring points were labeled A(1000 W), B(1250 W), C(1500 W), D(1750 W), and E(2000 W).

Figure 10(a) shows the temperature change curve of the monitoring points over time. The maximum temperature of the monitoring point was computed as 1281.8 °C, 1301.309 °C, 1317 °C, 1311.592 °C, and 1291.192 °C which were close to but below the melting point of high entropy alloy (1337 °C) [28]; therefore, it was interpreted as the horizontal direction of the melt pool border line. The model of powdered alloy was split into cube with 1 mm side lengths. Due to the symmetric model, the width of the melt pool was multiplied by 2 at the time of calculation. The width of the molten pool with various laser intensities was calculated to be 2.0 mm, 2.0 mm, 2.2 mm, 2.6 mm, and 2.6 mm, respectively. It can be observed that when laser power increases, the width of the melt layer also increases.

Figure 11 shows the temperature field cloud diagram in the depth direction. The monitoring points were labeled F(1000 W), G(1250 W), H(1500 W), I(1750 W), and J(2000 W). Figure 9(b) shows the temperature variation over time. The maximum monitoring point temperatures were calculated as 1297.15 °C, 1255.156 °C, 1272.806 °C, 1319.8 °C, and 1397.288 °C, which was lower than the melting point of 304 stainless steel (1398 °C). Due to the tetrahedral meshing of the substrate, the depth orientation spacing of the mesh is 0.086 mm. The depth of the molten pool was estimated to be around 0.334 mm, 0.334 mm, 0.43 mm, 0.43 mm, and 0.516 mm. As the laser intensity continued to increase, the depth of the melting pool was observed to expand. The formula for the laser energy density is as follows:

$$E = \frac{P}{DV} \quad (17)$$

where P is the laser power, D is the spot diameter, and V is the laser scanning speed.

The stronger the laser power is, the larger the heat input when the laser scanning speed and spot radius are known. Therefore, as the laser power increased, the width and depth of the melt pool also kept increasing.

In order to investigate the influence law of laser cladding process parameters on the morphology of the clad layer, the data was displayed in Fig. 12(a) which were fitted with a curve. It was a polynomial curve fit for width

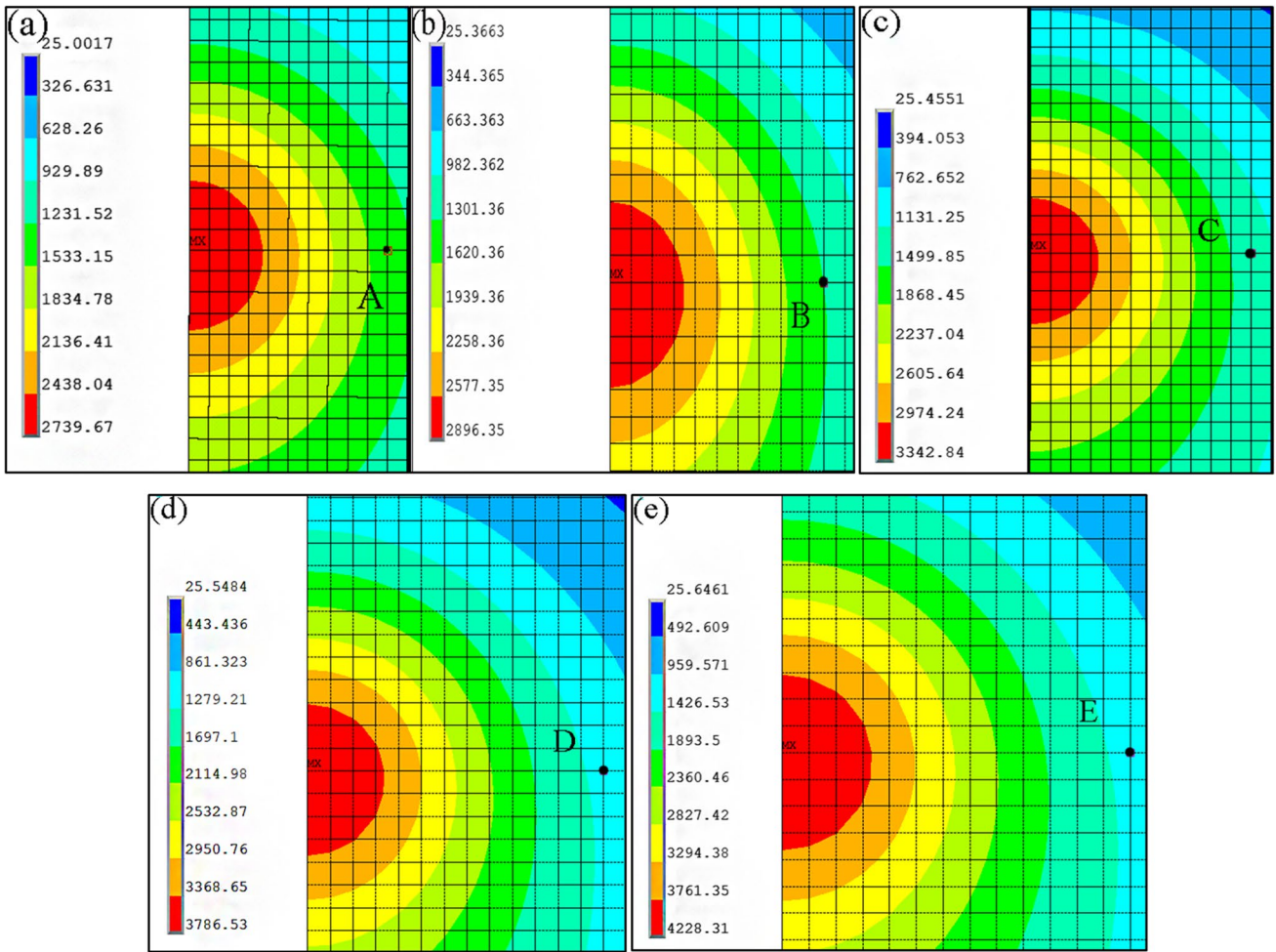


Fig. 9 Temperature measurement points along the width of the molten pool boundary at different laser powers and the same scanning speed of 10 mm/s: **a** 1000 W, **b** 1250 W, **c** 1500 W, **d** 1750 W, **e** 2000 W

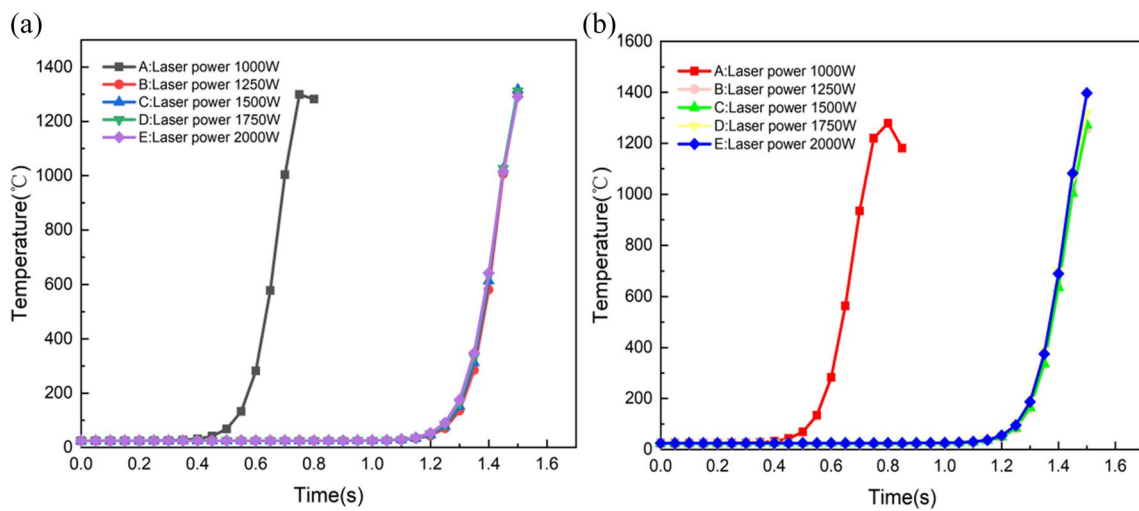


Fig. 10 Time process curves of temperature variation at the molten pool’s boundary measurement locations at various laser powers: **a** width direction, **b** depth direction

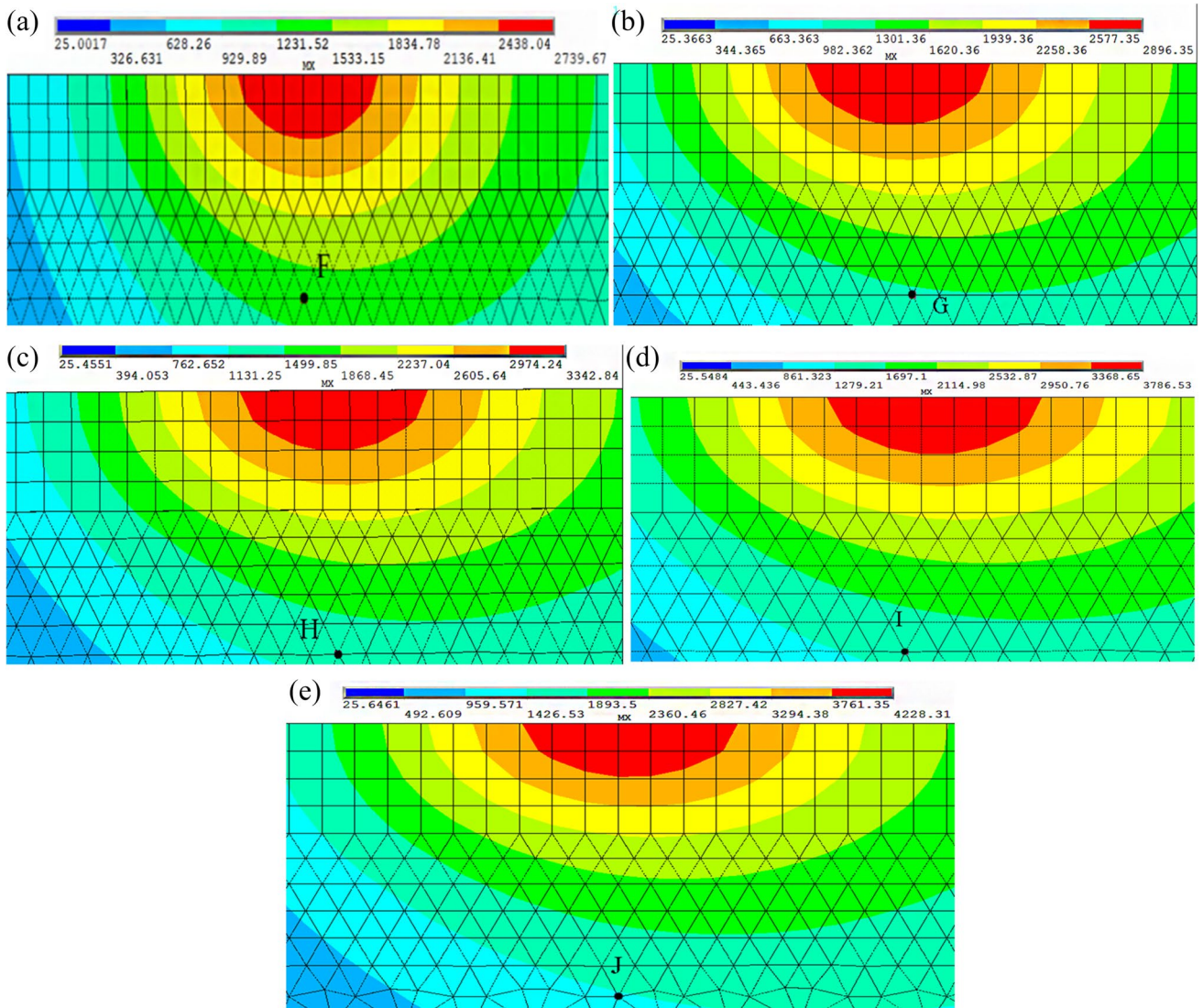


Fig. 11 Temperature measurement point along depth at the molten pool boundary at different laser power and the same scanning speed of 10 mm/s: **a** 1000 W, **b** 1250 W, **c** 1500 W, **d** 1750 W, **e** 2000 W

and depth at various laser strengths, with mean squared variances of 0.0748 and 0.092, respectively. It can be seen from Fig. 12(a), the depth and width of the molten pool is related to its laser power. Additionally, the width of the molten pool was more impacted by the laser intensity than its depth.

4.2 Effect of laser scanning speed on melt pool morphology

The horizontal monitoring points under different scanning speed were labeled K(5 mm/s), L(7.5 mm/s), M(10 mm/s), and N(12.5 mm/s) as shown in Fig. 13. The temperature curve of the horizontal monitoring point is displayed in

Fig. 14(a). The maximum temperatures of the monitoring points were 1312.226 °C, 1209.7 °C, 1317 °C, and 1226.9 °C, all of which were lower than the melting point of the high entropy alloy (1337 °C) [28]. The melt pool width was determined to be around 2.8 mm, 2.6 mm, 2.2 mm, and 2.2 mm. As the scanning speed increased, the breadth of the pool of melted decreased.

Figure 15 shows depth-directed temperature field cloud plot under different scanning speed. Observation sites were labeled O(5 mm/s), P(7.5 mm/s), Q(10 mm/s), and R(12.5 mm/s). And the temporal temperature trends are depicted in Fig. 14(b). The maximum temperatures recorded at the monitoring stations were lower than the melting point of 304 stainless steel (1398 °C). The depth of the melt pool

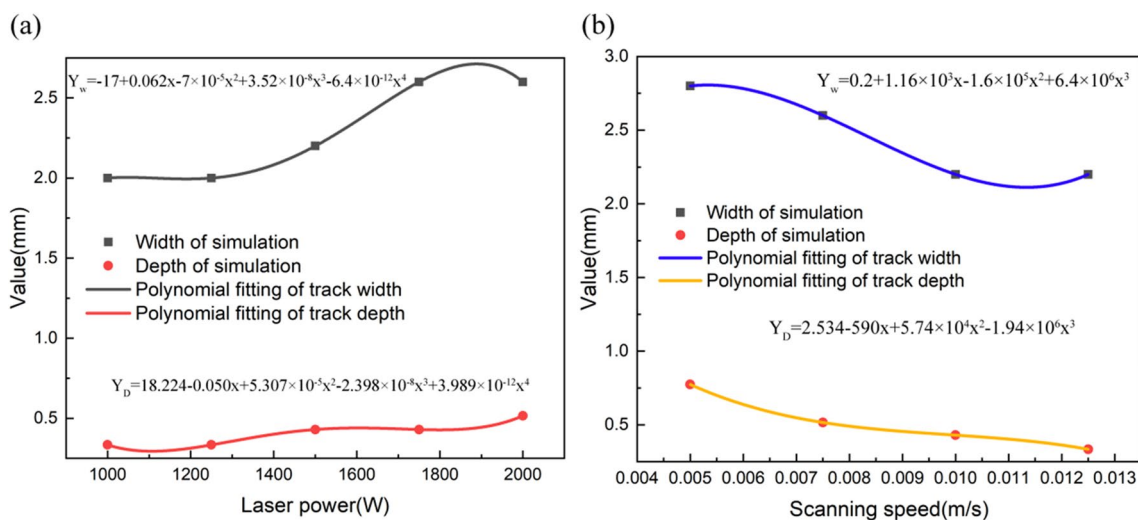
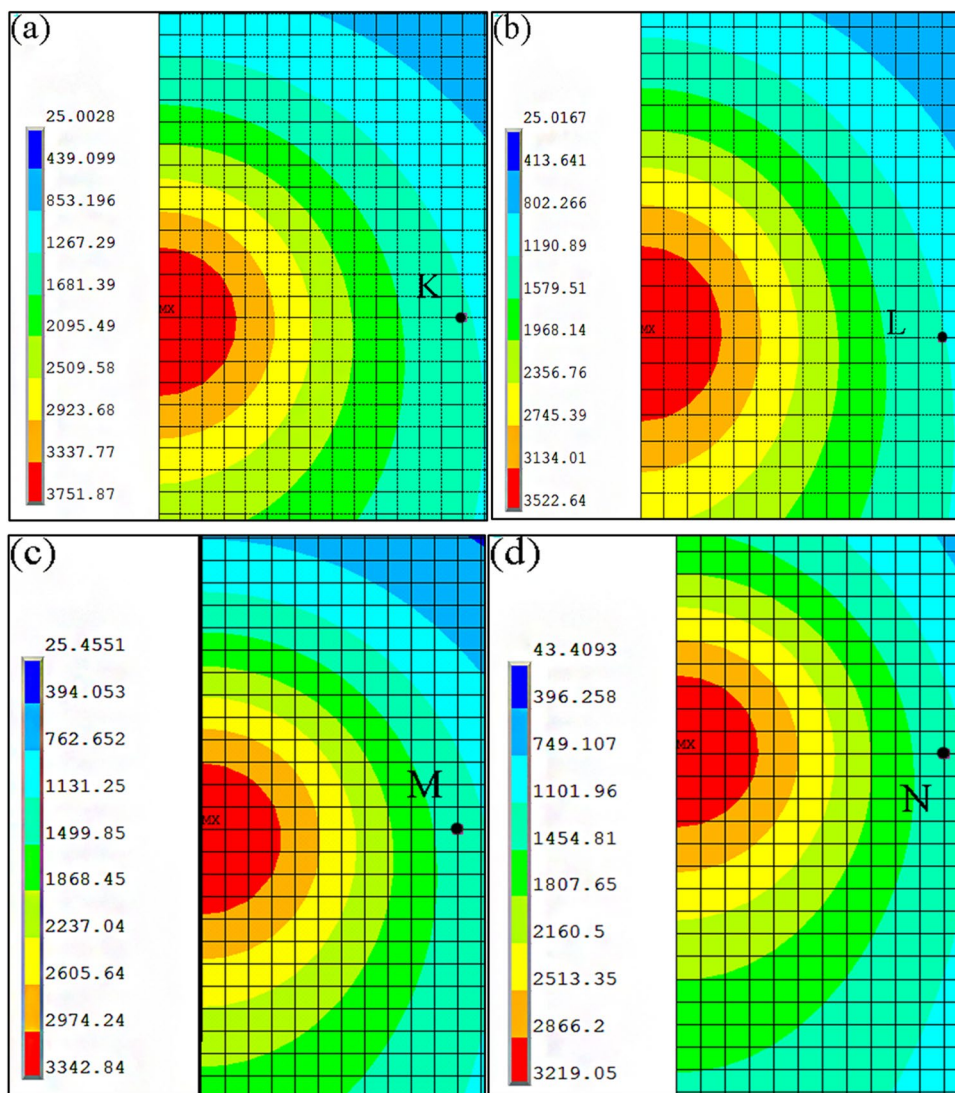


Fig. 12 Track width and depth with different process parameters: **a** laser power; **b** scanning speed

Fig. 13 Temperature measurement point along the width of the molten pool boundary at different scanning speeds at the same laser power of 1500 W: **a** 5 mm/s, **b** 7.5 mm/s, **c** 10 mm/s, **d** 12.5 mm/s



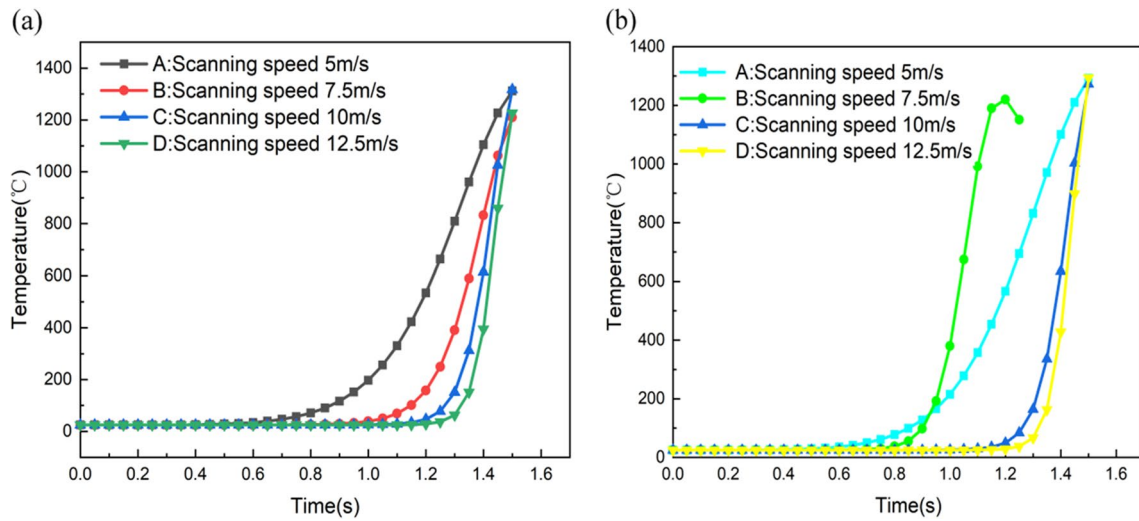


Fig. 14 Time process curves of temperature variation at the molten pool’s boundary measurement locations at different scanning speeds: **a** width direction; **b** depth direction

was calculated to be approximately: 0.774 mm, 0.516 mm, 0.43 mm, and 0.334 mm, indicating that as the scanning speed increased, the breadth and depth of the melt pool decreased.

Figure 12(b) shows a polynomial curve fit for width versus depth at different scanning speeds with mean squared deviations of 0.0871 and 0.092. From the fitting curve, it can be seen

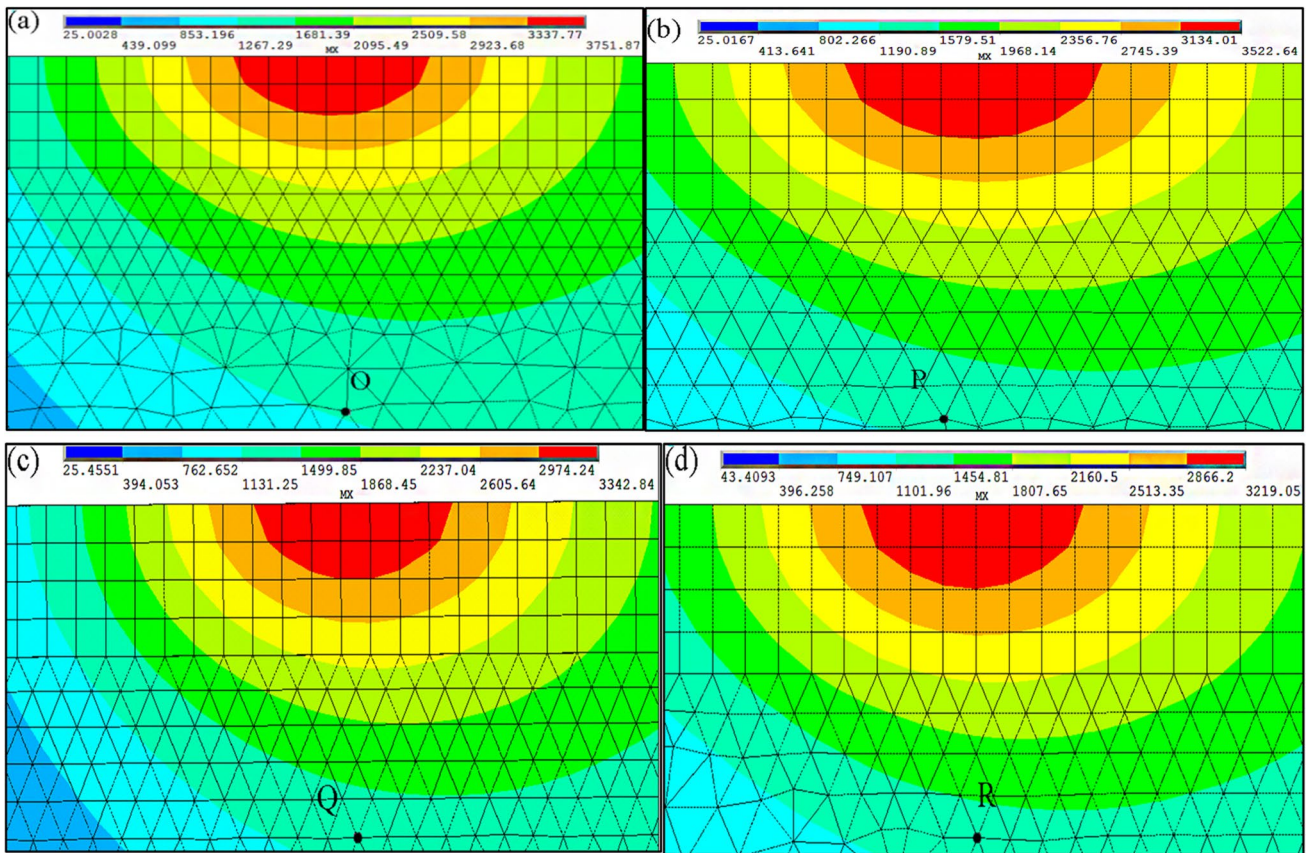
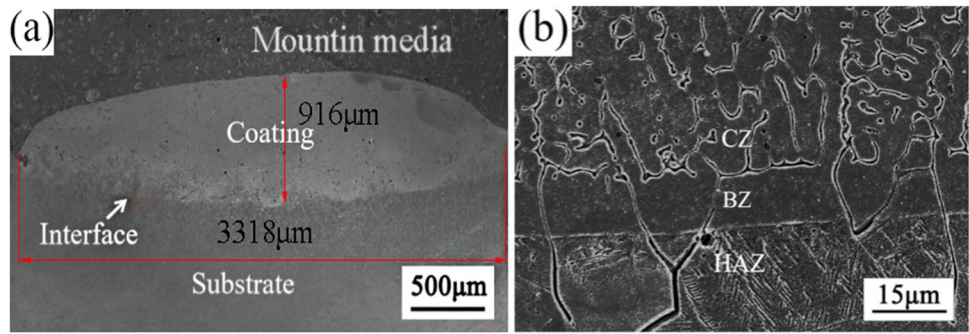


Fig. 15 Temperature measurement point of the molten pool boundary in the depth direction at different scanning speeds at the same laser power of 1500 W: **a** 5 mm/s, **b** 7.5 mm/s, **c** 10 mm/s, **d** 12.5 mm/s

Fig. 16 The microstructure of the CoCrCuFeNiSi0.1 HEA coatings: **a** cross-sections; **b** bonding zone



that the depth of the molten pool is inversely proportional to the width and sweep speed.

To test the accuracy of the model, several thermal and physical parameters of CoCrCuFeNiSi0.1 were utilized. Figure 16(a) shows that a good metallurgical bond is achieved between the coating and the substrate. The width and depth of the molten pool were measured to be about 3.3318 mm and 0.918 mm. It can be seen from Fig. 16(b) that the coating was divided into

three distinct areas from top to bottom: cladding zone (CZ), bonding zone (BZ), and heat-affected zone (HAZ), and the bond between these three regions were very tight. Above the bonding zone was a typical columnar crystal morphology, which grew perpendicular to the bonding surface and reversed the direction of thermal transfer toward the inside of the coating. The reason for this morphology is that a large temperature gradient was created between the coating and the matrix during the cladding process. And the internal temperature gradient was the large, the easier it was to form columnar crystals when the alloy solidifies. It can also be seen from Fig. 16(b) that the temperature gradient between the coating and the matrix was large, which was basically consistent with the experimental results.

Figure 17 shows the width and depth of the simulated coating. The comparison revealed that the width of the prediction is about 3.06 mm and the error is 7.77%, while the depth of the prediction is about 9.69 mm and the error is 5.78%. There were some errors in the forecast results due to the neglect of the liquid flow in the molten pool, evaporative heat loss, and non-melting heat transfer, while the thermal properties of the material were calculated by software, which has errors at high temperatures. Finally, in this paper, the boundary point of the melt pool is established at the grid junction point to facilitate the calculation. In order to obtain the melt pool boundary more accurately, the selection of melt pool boundaries can no longer be limited to the cell nodes.

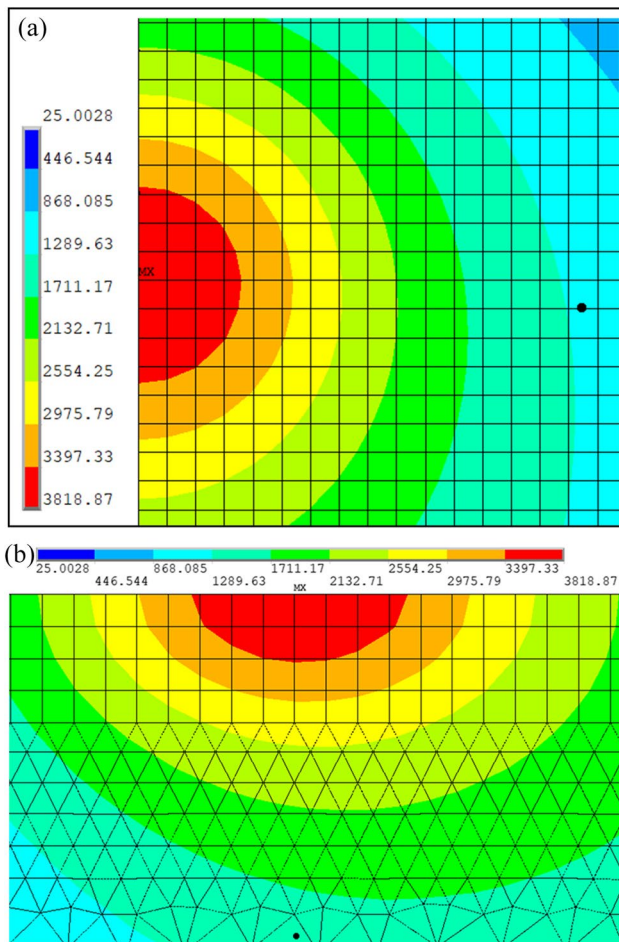


Fig. 17 High entropy alloy cladding layer shape prediction: **a** width of the simulation; **b** depth of simulation

5 Conclusion

Using a single-track laser cladding model with an asymmetric Gaussian heat source and temperature discrimination mechanism, the temperature variation of the 304 stainless steel laser cladding process was studied, the data was curve-fitted, and the melt pool morphology changes were predicted, leading to the following results:

- 1 The heat source’s core temperature was the highest due to the Gaussian distribution of the laser heat source, and the molten pool had an elliptical form. The temper-

ature gradient was smallest in the center of the molten pool and gradually increased as it moves outward.

- 2 Temperature–time analysis was performed on the laser scanning path nodes. The initial maximum temperature of the node continued to increase. As the laser scanning progressed, the maximum temperature reached its peak and the node's temperature curve tends to become increasingly stable.
- 3 The width and depth of the pool were adapted for various laser powers. Due to the fact that laser power directly influences the heat input, the breadth and depth of the melt pool and the laser were proportionate to laser power based on the fitting results. The laser power had a higher impact on the width of the molten pool than on its depth.
- 4 Curve fitting of the width and depth of the melt pool at various scanning speeds revealed that as the laser scanning speed increases, the width and depth of the melt pool continue to decrease, which was due to the decrease in heat accumulation time. Simulated and experimental results were compared, which largely matched the experimental measurements.

Acknowledgements This work was financially supported by the National Natural Science Foundation of China (51402189) and Class III Peak Discipline of Shanghai-Materials Science and Engineering (High-Energy Beam Intelligent Processing and Green Manufacturing).

Author contribution Dachuan Tian: conceptualization, methodology, software, writing—original draft, visualization, investigation. Chonggui Li: conceptualization, methodology, software, writing—original draft, review and editing. Zhiguo Hu: supervision, formal analysis, software, validation. Xintong Li: visualization, investigation. Yajun Guo: visualization, investigation. Xiaosong Feng: writing—review and editing. Zhenhai Xu: writing—review and editing. Xiaoguang Sun: writing—review and editing. Wenge Li: writing—review and editing.

Funding National Natural Science Foundation of China (51402189) and Class III Peak Discipline of Shanghai-Materials Science and Engineering (High-Energy Beam Intelligent Processing and Green Manufacturing).

Declarations

Competing interests The authors declare no competing interests.

References

1. Taiwade RV, Patil AP, Ghugal RD, Patre SJ, Dayal RK (2013) Effect of welding passes on heat affected zone and tensile properties of AISi 304 stainless steel and chrome-manganese austenitic stainless steel. *ISIJ Int* 53:102–109
2. Xing X, Han Z, Wang H, Lu P (2015) Electrochemical corrosion resistance of ceo₂-cr/ti coatings on 304 stainless steel via pack cementation. *J Rare Earths* 33:1122–1128
3. Kai G, Wang Z, Ming G, Li X, Zeng X (2013) Effects of processing parameters on tensile properties of selective laser melted 304 stainless steel. *Mater Des* 50:581–586
4. Martins CMB, Moreira JL, Martins JI (2014) Corrosion in water supply pipe stainless steel 304 and a supply line of helium in stainless steel 316. *Eng Failure Anal* 39:65–71
5. Liverani E, Toschi S, Ceschini L, Fortunato A (2017) Effect of selective laser melting (SLM) process parameters on microstructure and mechanical properties of 316L austenitic stainless steel. *J Mater Process Technol* 249:255–263
6. Cheng JB, Liang XB, Wang ZH, Xu BS, Chem P (2013) formation and mechanical properties of CoNiCuFeCr high-entropy alloys coatings prepared by plasma transferred arc cladding process. *Plasma Chem Plasma Process* 33:979–992
7. Hsu YJ, Chiang WC, Wu JK (2005) Corrosion behavior of FeCoNiCrCu high-entropy alloys in 3.5% sodium chloride solution. *Mater Chem Phys* 92:112–117
8. Praveen S, Murty BS, Kottada RS (2012) Alloying behavior in multi-component AlCoCrCuFe and NiCoCrCuFe high entropy alloys. *Mater Sci Eng A-Struct* 534:83–89
9. Chang HT, Huo XF, Li WP, Yang T, Huang JC, Wu BL, Duan GS, Du XH (2020) Research development of strengthening mechanism of high entropy alloy. *Rare Met Mat Eng* 49:3633–3645
10. Jin G, Cai Z, Guan Y, Cui X, Liu Z, Li Y, Dong ML, Zhang D (2018) High temperature wear performance of laser-cladded fenicoalco high-entropy alloy coating. *Appl Surf Sci* 445:112–113
11. Wang FJ, Zhang Y (2008) Effect of Co addition on crystal structure and mechanical properties of Ti0.5CrFeNiAlCo high entropy alloy. *Mater Sci Eng A* 496:214–216
12. Devojno OG, Feldshtein E, Kardapolava MA, Lutsko NI (2018) On the formation features, microstructure and microhardness of single laser tracks formed by laser cladding of a niobium self-fluxing alloy. *Opt Laser Eng* 106:32–38
13. Huang YL, Zou DN, Liang GY, Su JY (2003) Numerical simulation on cladding track, fluid flow field and temperature field in laser cladding process with powder feeding. *Rare Met Mat Eng* 5:330–334
14. Liu CM, Li CG, Zhang Z, Sun S, Zeng M, Wang FF, Guo YJ, Wang JQ (2020) Modeling of thermal behavior and microstructure evolution during laser cladding of AlSi10Mg alloys. *Opt Laser Technol* 123:105926
15. Li RF, Jin YJ, Li ZG, Zhu YY, Wu MF (2014) Effect of the remelting scanning speed on the amorphous forming ability of Ni-based alloy using laser cladding plus a laser remelting process. *Surf Coat Technol* 259:725–731
16. Marzban J, Ghaseminejad P, Ahmadzadeh MH, Teimouri R (2015) Experimental investigation and statistical optimization of laser surface cladding parameters. *Int J Adv Manuf Technol* 76:1163–1172
17. Hao M, Sun Y (2013) A fem model for simulating temperature field in coaxial laser cladding of ti6al4v alloy using an inverse modeling approach. *Int J Heat Mass Transfer* 64:352–360
18. Lei YW, Sun RL, Ying T, Wei N (2012) Numerical simulation of temperature distribution and tic growth kinetics for high power laser clad tic/nicrbsic composite coatings. *Opt Laser Technol* 44:1141–1147
19. Gao GL, Wu CZ, Hao YB, Xu XC, Guo LG (2020) Numerical simulation and experimental investigation on three-dimensional modelling of single-track geometry and temperature evolution by laser cladding. *Opt Laser Technol* 129:106287
20. Hofman JT, De Lange DF, Pathiraj B, Meijer J (2011) FEM modeling and experimental verification for dilution control in laser cladding. *J Mater Process Technol* 49:187–196
21. Velaga SK, Ravisankar A (2017) Finite element based parametric study on the characterization of weld process moving heat source parameters in austenitic stainless steel. *Int J Pressure Vessels Piping* 157:63–73

22. Guo YJ, Li CG, Zeng M, Wang JQ, Deng PR, Wang Y, Zhang YF (2020) In-situ TiC reinforced CoCrCuFeNiSi0.2 high-entropy alloy coatings designed for enhanced wear performance by laser cladding. *Mater Chem Phys* 242:122522
23. Gusarov AV, Smurov I (2010) Modeling the interaction of laser radiation with powder bed at selective laser melting. *Physcs Proc* 5:381–394
24. Gusarov AV, Laoui T, Froyen L, Titov VI (2003) Contact thermal conductivity of a powder bed in selective laser sintering. *Int J Heat Mass Tran* 46:1103–1109
25. Du L, Gu DD, Dai DH, Shi QM, Ma CL, Xia MJ (2018) Relation of thermal behavior and microstructure evolution during multi-track laser melting deposition of Ni-based material. *Opt Laser Technol* 108:207–217
26. Gan Z, Yu G, He X, Li SX (2017) Numerical simulation of thermal behavior and multicomponent mass transfer in direct laser deposition of Co-base alloy on steel[J]. *Int J Heat Mass Transf* 104:28–38
27. Sun D, Tong YG, Hen XN (2010) Research on the influencing factors of laser absorption rate in laser welding[J]. *Hot Working Technol* 19:165–167
28. Wang WL, Hu L, Luo SB, Meng LJ, Geng DL, Wei B (2016) Liquid phase separation and rapid dendritic growth of high-entropy CoCrCuFeNi alloy. *Intermetallics* 77:41–45

Publisher's Note Springer Nature remains neutral with regard to jurisdictional claims in published maps and institutional affiliations.

Springer Nature or its licensor (e.g. a society or other partner) holds exclusive rights to this article under a publishing agreement with the author(s) or other rightsholder(s); author self-archiving of the accepted manuscript version of this article is solely governed by the terms of such publishing agreement and applicable law.